cessfully within a range of interaction values. The fact that there exists a window of tolerance suggests the possibility of added room for experimental optimization to generate lower defect densities or even higher orders of density multiplication. For instance, it should be possible to change the brush layer to optimize the brush interactions in density multiplied patterns with L_s = 54 nm in order to reduce the defect density below 10^{-4} (see Moiré patterns in fig. S2).

A technological benchmark for the quality of the patterns is garnered from transferring the pattern to the underlying substrate. The block copolymer film produced by density multiplication has a vertical side-wall profile suitable for pattern transfer. Using a lift-off technique, we fabricated 20-nm-tall Si pillars. We started with a block copolymer film like the one shown in Fig. 2F (L_s = 78 nm, L_p = 39 nm) after removing the PMMA cylinder and cleaned the pores with oxygen plasma. We deposited 7 nm of Cr by e-beam evaporation and removed the PS mask using a piranha solution leaving Cr dots on the surface (Fig. 4A). We used a CF_4 reactive ion etch to generate 20-nm Si pillars (Fig. 4B). The pillars were uniform over the entire sample (3 mm long) and otherwise identical to those formed in patterns where L_s = 39 nm. Taken together, molecular simulation and pattern transfer results demonstrate that the degree of perfection, registration, and vertical side-wall profiles of the enhanced-resolution templates provide a path based on e-beam patterning and directed assembly of block copolymers toward bit-patterned media at densities over 1 Tb/in^2.

We envision the role of directed assembly to enhance, augment, and advance the performance of lithographic processes rather than to attempt to develop replacement technology. The starting point is a chemical prepattern at or near the limit of current lithographic tools to provide strong thermodynamic driving forces for directed assembly of patterns with perfection, registration, resolution, and quality beyond those possible with traditional materials and processes. In this context, we anticipate that the experiments here with cylindrical-phase diblock copolymers could be extended to higher-density multiplication factors for patterned media and to other classes of block copolymers to achieve striped or more complex patterns such as those required by the semiconductor industry.

References and Notes

1. Semiconductor Industry Association, *International Technology Roadmap for Semiconductor, 2005 Edition* (Semiconductor Industry Association, San Jose, CA, 2005).
2. D. J. C. Herr, *Future Fab. Int.* **20**, 82 (2006).
3. B. D. Terris, T. Thomson, *J. Phys. D Appl. Phys.* **38**, R199 (2005).
4. C. Ross, *Annu. Rev. Mater. Res.* **31**, 203 (2001).
5. D. Weller, A. Moser, *IEEE Trans. Magn.* **35**, 4423 (1999).
6. F. S. Bates, G. H. Fredrickson, *Annu. Rev. Phys. Chem.* **41**, 525 (1990).
7. M. J. Park *et al.*, *Nano Lett.* **7**, 3547 (2007).
8. C. T. Black *et al.*, *IBM J. Res. Develop.* **51**, 605 (2007).
9. C. T. Black, *Acs Nano* **1**, 147 (2007).
10. S. O. Kim *et al.*, *Nature* **424**, 411 (2003).
11. M. P. Stoykovich *et al.*, *Science* **308**, 1442 (2005).
12. R. A. Segalman, H. Yokoyama, E. J. Kramer, *Adv. Mater.* **13**, 1152 (2001).
13. S. H. Kim, M. J. Misner, T. P. Russell, *Adv. Mater.* **16**, 2119 (2004).
14. G. Hadziioannou, A. Mathis, A. Skoulios, *Colloid Polym. Sci.* **257**, 136 (1979).
15. A. Keller, E. Pedemont, F. M. Willmout, *Nature* **225**, 538 (1970).
16. T. Thurn-Albrecht *et al.*, *Science* **290**, 2126 (2000).
17. T. Hashimoto *et al.*, *Polymer* **39**, 1573 (1998).
18. B. C. Berry, A. W. Bosse, J. F. Douglas, R. L. Jones, A. Karim, *Nano Lett.* **7**, 2789 (2007).
19. T. Hashimoto, J. Bodycomb, Y. Funaki, K. Kimishima, *Macromolecules* **32**, 952 (1999).
20. S. H. Kim *et al.*, *Macromolecules* **39**, 8473 (2006).
21. E. W. Edwards, M. F. Montague, H. H. Solak, C. J. Hawker, P. F. Nealey, *Adv. Mater.* **16**, 1315 (2004).
22. K. O. Stuen *et al.*, *J. Vac. Sci. Technol. B* **25**, 1958 (2007).
23. The chemical patterns are written on a rectangular lattice and not on a hexagonal lattice because the e-beam moves in an *x-y* grid with discrete steps along the *x* and *y* axis. The e-beam prepattern consists of a rectangular lattice with two dots in the unit cell that are the closest match to the natural hexagonal lattice of the block copolymer.
24. T. Thurn-Albrecht *et al.*, *Adv. Mater.* **12**, 787 (2000).
25. R. A. Segalman, A. Hexemer, E. J. Kramer, *Phys. Rev. Lett.* **91**, 196101 (2003).
26. K. C. Daoulas *et al.*, *Langmuir* **24**, 1284 (2008).
27. E. W. Edwards *et al.*, *Macromolecules* **40**, 90 (2007).
28. K. C. Daoulas *et al.*, *Phys. Rev. Lett.* **96**, 036104 (2006).
29. S. M. Park, G. S. W. Craig, Y. H. La, H. H. Solak, P. F. Nealey, *Macromolecules* **40**, 5084 (2007).
30. F. Detcheverry, H. Kang, K. C. Daoulas, M. Muller, P. F. Nealey, *Macromolecules* **41**, 4989 (2008).

31. We thank C. P. Henderson, B. Marchon (Hitachi GST), and H. Yoshida (Hitachi Ltd.) for insightful discussions. This research was supported by Hitachi Global Storage Technologies Inc., the Semiconductor Research Corporation, and the National Science Foundation through the University of Wisconsin Nanoscale Science and Engineering Center (MPS/DMR-0425880). Patent protection related to this work is pending.

Supporting Online Material

www.sciencemag.org/cgi/content/full/321/5891/936/DC1
Materials and Methods
Figs. S1 and S2
References

11 March 2008; accepted 27 June 2008
10.1126/science.1157626

Graphoepitaxy of Self-Assembled Block Copolymers on Two-Dimensional Periodic Patterned Templates

Ion Bita,[1]*† Joel K. W. Yang,[2]* Yeon Sik Jung,[1]* Caroline A. Ross,[1]‡ Edwin L. Thomas,[1]‡ Karl K. Berggren[2]‡

Self-assembling materials are the building blocks of bottom-up nanofabrication processes, but they need to be templated to impose long-range order and eliminate defects. In this work, the self-assembly of a thin film of a spherical-morphology block copolymer is templated using an array of nanoscale topographical elements that act as surrogates for the minority domains of the block copolymer. The orientation and periodicity of the resulting array of spherical microdomains are governed by the commensurability between the block copolymer period and the template period and is accurately described by a free-energy model. This method, which forms high-spatial-frequency arrays using a lower-spatial-frequency template, will be useful in nanolithography applications such as the formation of high-density microelectronic structures.

Self-assembly of nanometer-length-scale patterns in two dimensions (2D) is currently of interest as a method for improving throughput and resolution in nanolithography. Self-assembly in 2D has been studied widely in a range of systems, including self-assembled monolayers (*1*), quantum dots (*2*), and colloidal particles (*3*). Among these systems, the self-assembly of thin films of block copolymers (BCPs) has many attractive aspects resulting from the intrinsic ability of BCPs to generate uniform and periodic nanoscale structures in parallel over large areas by microphase separation (*4*). BCP thin films with spherical, cylindrical, or lamellar morphologies of different length scales may be created by adjusting the composition and molecular weight of the BCP. These morphologies can be employed for the fabrication of nanostructures: After selectively removing one of the blocks, the remaining pattern can be transferred into a functional material (*5*–*10*). However, the spontaneous process of microphase separation leads to the formation of "polycrystalline" BCP microdomain arrays consisting of randomly oriented ordered regions, or grains, which limits the potential applications. This issue has sparked the development of a host of techniques that attempt to control the ordering of thin-film BCP systems, that is, to template the positions of the microdomains and to form "single-crystal" structures

[1]Department of Materials Science and Engineering, Massachusetts Institute of Technology, 77 Massachusetts Avenue, Cambridge, MA 02139, USA. [2]Department of Electrical Engineering and Computer Science, Massachusetts Institute of Technology, 77 Massachusetts Avenue, Cambridge, MA 02139, USA.

*These authors contributed equally to this work.
†Present address: Qualcomm Micro Electro Mechanical Systems Technologies, 2581 Junction Avenue, San Jose, CA 95134, USA.
‡To whom correspondence should be addressed. E-mail: caross@mit.edu (C.A.R.), elt@mit.edu (E.L.T.), berggren@mit.edu (K.K.B.)

in which the locations and orientations of the microdomains are precisely determined (*11*–*13*). These techniques include the use of topographically (*14*–*16*) or chemically (*17*–*20*) patterned substrates as templates for the self-assembly process. Recent work has extended the chemical patterning technique such that templates with a period of up to four times that of the BCP could be used to produce large-area defect-free lamellar or cylindrical domain patterns (*21*, *22*).

We describe here a topographical graphoepitaxy technique for controlling the self-assembly of BCP thin films that produces 2D periodic nanostructures with a precisely determined orientation and long-range order. The surface of the substrate is patterned with a sparse 2D lattice of nanoscale posts designed to act as surrogate spherical or cylindrical domains of the minor component of the BCP. Each of these posts is designed to be chemically and physically nearly indistinguishable from the BCP entity (the microdomain and its associated corona) for which it substitutes. This approach differs from previous approaches, which used linear substrate steps or grooves (*12*, *16*), in that here the discrete posts are distributed over the substrate, providing a set of periodic constraints that interact both locally and globally with the array of BCP domains.

The BCP used in our experiments was spherical-morphology polystyrene-*b*-polydimethylsiloxane (PS-*b*-PDMS) with molecular weight = 51.5 kg/mol, minority block volume fraction f_{PDMS} = 16.5%, and polydispersity (PDI) = 1.04. This BCP was chosen because it has both a high Flory-Huggins χ-parameter, giving a large driving force for microphase segregation, and a high chemical selectivity between the two blocks for subsequent pattern transfer. The BCP was spin-coated to a thickness of ~50 nm and annealed at 200°C to obtain a monolayer of 20-nm-diameter PDMS spheres with a center-to-center spacing of 40 nm within a PS matrix [see supporting online material (SOM), section S1]. In this process, a surface layer of PDMS forms at the substrate-BCP and BCP-air interfaces due to the low surface energy of PDMS (*10*). By using CF_4 followed by oxygen reactive-ion etching (RIE), the PS matrix was selectively removed to reveal the oxidized PDMS spherical microdomains (*10*).

To template the BCP, we used a sparse 2D array of posts created by scanning-electron-beam lithography of a 40-nm-thick hydrogen silsesquioxane (HSQ) resist layer on a Si substrate. HSQ is a radiation-sensitive spin-on-glass that forms a silica-like material directly upon electron-beam exposure. Development reveals the exposed posts, without requiring further etching or

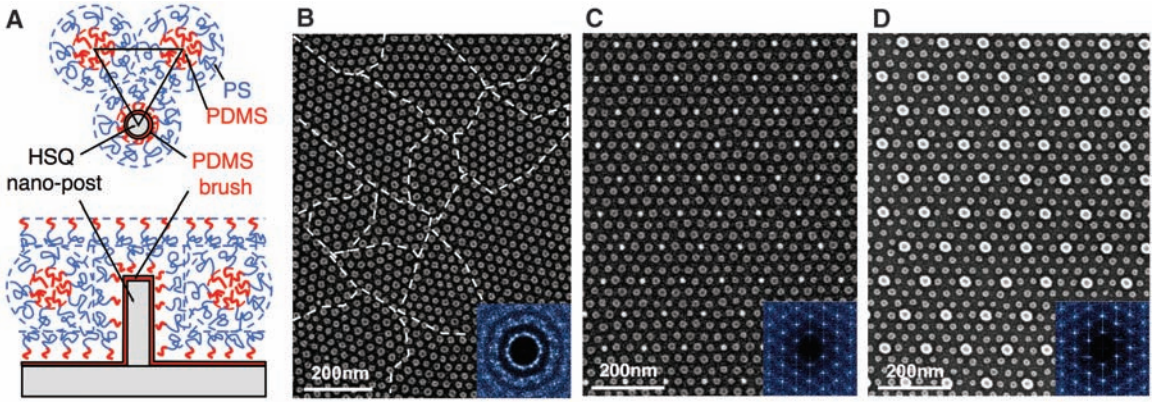

Fig. 1. (**A**) Top-down and side-view schematics showing the arrangement of PS-*b*-PDMS block copolymer molecules in the region surrounding a single post made from cross-linked HSQ resist. The post and substrate surfaces have been chemically functionalized by a monolayer of short-chain PDMS brush. (**B**) SEM images of a poorly ordered monolayer of BCP spherical domains formed on a flat surface, that is, without templating. The boundaries between different grain orientations are indicated with dashed lines. The inset is a 2D Fourier transform of the domain positions that shows the absence of long-range order. (**C** and **D**) SEM images of ordered BCP spheres formed within a sparse 2D lattice of HSQ posts (brighter dots). The substrate and post surfaces were functionalized with a PDMS brush layer in (C), which corresponds to the schematic in (A), and with a PS brush layer in (D). The insets show the 2D Fourier transforms in which the low-frequency components originate from the post lattice.

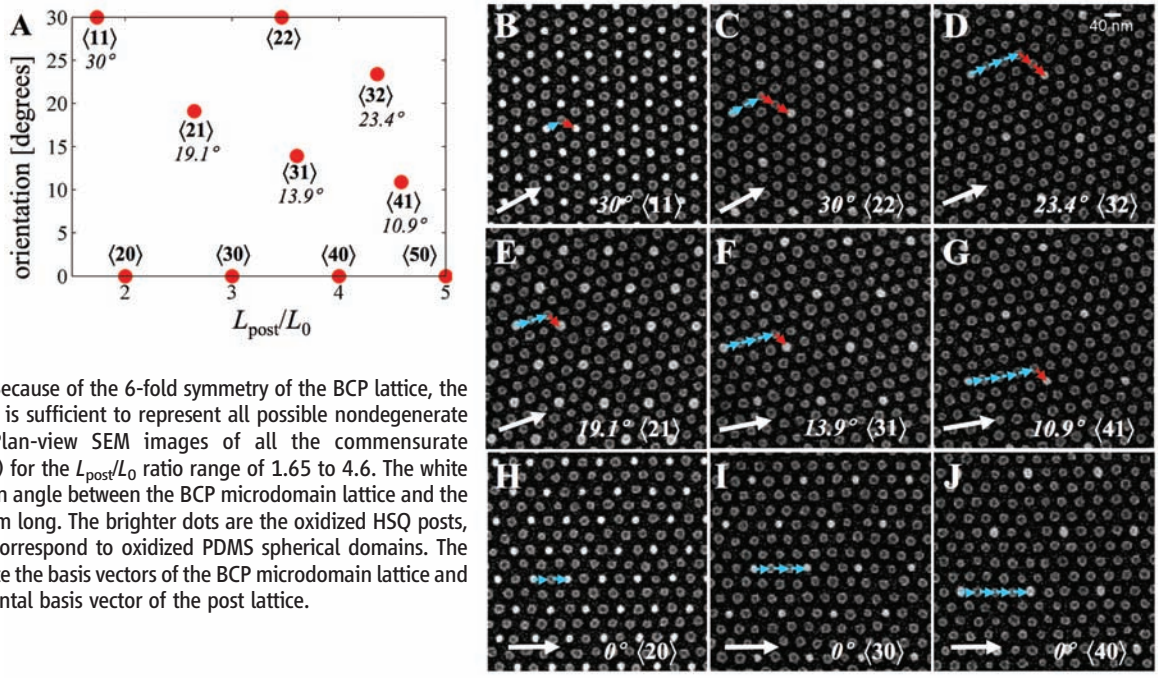

Fig. 2. (**A**) Calculated orientations at which the BCP microdomain lattice is commensurate with the post lattice, as a function of L_{post}/L_0. The BCP lattice is commensurate with the post lattice when the post lattice basis vectors of length L_{post} can be represented as integer multiples, <*ij*>, of the BCP lattice basis vectors of equilibrium length L_0. Because of the 6-fold symmetry of the BCP lattice, the angular span of 0° to 30° is sufficient to represent all possible nondegenerate orientations. (**B** to **J**) Plan-view SEM images of all the commensurate configurations found in (A) for the L_{post}/L_0 ratio range of 1.65 to 4.6. The white arrows show the orientation angle between the BCP microdomain lattice and the post lattice and are 120 nm long. The brighter dots are the oxidized HSQ posts, whereas the darker dots correspond to oxidized PDMS spherical domains. The blue and red arrows indicate the basis vectors of the BCP microdomain lattice and add up to form one horizontal basis vector of the post lattice.

processing. A key requirement for this process is for the surface of the posts to exhibit preferential affinity toward one of the domains of the BCP, which was established by chemical functionalization of the template surface using hydroxy-terminated homopolymer PS or PDMS brushes. Figure 1A illustrates the topographic and chemical design of the posts used in most of our experiments. The template was functionalized with a short PDMS homopolymer brush, and a post substitutes for a PDMS sphere in the close-packed array. The template can also be fabricated with an affinity toward the majority block by using a PS brush, which requires larger-diameter HSQ. PDMS brush-coated substrates provided better ordering of PS-*b*-PDMS microdomain arrays than PS-coated or uncoated substrates, which we attributed to higher surface diffusivity of the PDMS brush (*10*). The use of PDMS brush-coated posts, which required the ability to fabricate ~10-nm structures lithographically, was enabled by recent high-resolution development methods in electron-beam lithography (*23*).

Figure 1, C and D, shows that appropriately sized and functionalized posts could template the assembly of a BCP lattice. For comparison, Fig. 1B shows the results of untemplated assembly for the same BCP. The template in Fig. 1C consisted of ~12-nm-diameter HSQ posts functionalized with PDMS (5 kg/mol) of thickness ~2 nm, resulting in a post diameter of ~16 nm. Figure 1D shows results from 20-nm-diameter HSQ posts functionalized with PS (10 kg/mol) of ~5 nm thickness, resulting in a post diameter of 30 nm.

We next considered the more general problem of how a sparse template could be designed to ensure the formation of a single-grain BCP lattice of controlled period and orientation. For a close-packed template of period L_{post}, and a close-packed BCP microdomain array of period $L <$ L_{post}, the commensurability between the BCP lattice and the template lattices depends on the ratio L_{post}/L. In the simplest case, where L_{post}/L is an integer, the lattice vectors of the template and the BCP sphere array are parallel, as seen in the scanning electron micrograph (SEM) images of Fig. 1, where $L_{post}/L = 3$, and θ, the angle between a post lattice basis vector and a BCP microdomain lattice basis vector, is zero. For noninteger values of L_{post}/L, however, a variety of commensurate BCP lattices with orientations $\theta \neq 0$ can occur. As shown in SOM section S2, when a basis vector of the post lattice is equal to the sum of integer multiples i and j of the two 60°-oriented basis vectors of the BCP microdomain lattice,

$$L_{post}/L = \sqrt{i^2 + j^2 + ij} \quad (1)$$

then the angle θ between the post lattice and BCP microdomain lattice is given by

$$\theta = \arccos\left(\frac{2i + j}{2\sqrt{i^2 + j^2 + ij}}\right) \quad (2)$$

We use a notation of the form $\langle i\, j\rangle$ to describe the possible commensurate BCP lattice configurations that can form within a post lattice. For example, the structures shown in Fig. 1C and 1D would be labeled as $\langle 3\ 0\rangle$ under this notation, indicating that a post lattice basis vector is parallel to a BCP microdomain lattice vector and three times as long. Figure 2A presents a map of the mathematically possible commensurate lattice configurations in which the L_{post}/L ratio was varied continuously up to $L_{post}/L = 5$. For each of these $\langle i\, j\rangle$ orientations, the number of microdomains templated by each post is given by $i^2 + j^2 + ij - 1$. For example, 8 BCP microdomains are templated per post for the $\langle 3\ 0\rangle$ lattice and 26 for the $\langle 3\ 3\rangle$ lattice. The post lattice is analogous to a coincident site lattice (CSL) of the BCP lattice, in which smaller $\langle i\, j\rangle$ values correspond to smaller CSL sigma values and a greater number of coincident post and BCP lattice sites. Figure 2, B to J, shows SEM images of all the commensurate orientations that we observed within the range $L_{post}/L = 1.65$ to 4.6. These orientations agree with the predictions in Fig. 2A.

BCP arrays may develop a tensile or compressive strain to fit within a template, as observed in confined spherical, cylindrical, or lamellar arrays (*18*, *24*). Confined BCP arrays are capable of exhibiting strain, with tension being easier to accommodate than compression (*25*). This compliance enables a greater number of configurations to be experimentally accessed at particular values of L_{post}/L than the discrete results in Fig. 2A would suggest. The ability of the BCP microdomain lattice to deform elastically therefore enables multiple BCP arrangements to form on a given post lattice, each with a different lattice parameter and orientation θ.

To predict the configuration(s) that will form, we consider a simple free energy model for the BCP microdomain array as a function of L_{post}/L. Given an $\langle i\, j\rangle$ configuration and a post spacing L_{post} such that the commensurate sublattice period L differs from the equilibrium spacing of the BCP on a flat substrate, L_0, the templated BCP may either assume a strained spacing and fit inside the post lattice, or form local defects and relieve the long-range stress. The free-energy change for straining the BCP lattice can be approximated under an affine deformation model by considering the effect of strain on both the conformational entropy of a polymer chain and the interfacial energy between the BCP domains. The derivation of the free-energy expression is described in SOM section S3 and leads to

$$\Delta F_{chain}/kT = \frac{2Mb}{L}\sqrt{\frac{\chi_{AB}}{6}} + \frac{1}{2}\left(\frac{L^2}{4Mb^2} + \frac{4b\sqrt{M}}{L} - 3\right) \quad (3)$$

where L is the strained BCP spacing required for the BCP lattice to be commensurate with the template for the considered $\langle i\, j\rangle$ configuration, M is the number of statistical segments of the BCP chain, b is the statistical segment length, χ_{AB} is the Flory-Huggins interaction parameter (*26*, *27*), k is Boltzmann's constant, ΔF_{chain} is the free energy per BCP chain, and T is the temperature. The equilibrium spacing L_0 was obtained by minimizing the free energy with respect to L. $\Delta F_{chain}/k\,T$ was then calculated for all the $\langle i\, j\rangle$ combinations by substituting $L = L_{post}/\sqrt{i^2 + j^2 + ij}$. These energy curves are plotted in Fig. 3A as a function of L_{post}/L_0. Each distinct $\langle i\, j\rangle$ lattice has an energy well with a minimum corresponding to the value of L_{post}/L_0

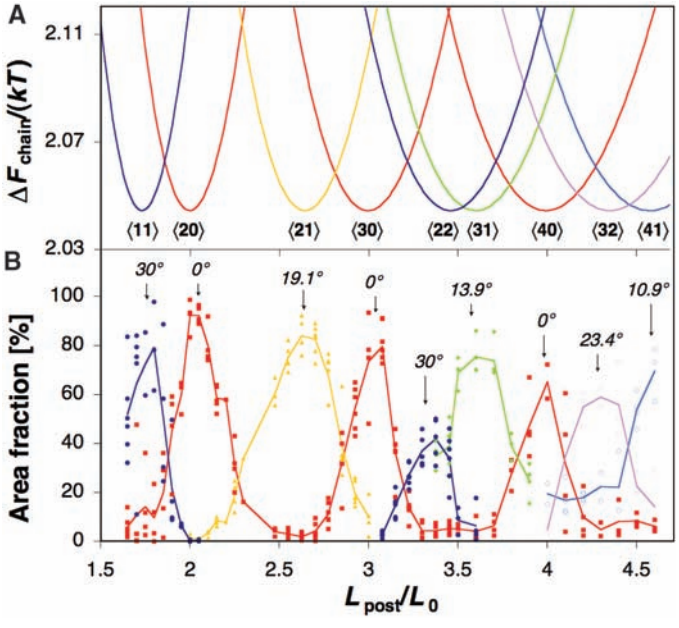

Fig. 3. (**A**) Theoretical prediction of free energy per BCP chain versus L_{post}/L_0 for each commensurate configuration. Free-energy minima occur at L_{post}/L_0 values where the commensurate condition is satisfied without straining the BCP microdomain array. (**B**) Experimental results showing the area fraction of each $\langle i\, j\rangle$ lattice versus L_{post}/L_0. Each filled circle is a data point obtained by image processing of an SEM image of a 1.3 μm by 1.3 μm square area of the templated region. This plot was generated from data collected from over 200 images of different post lattices on the same substrate. The solid lines connect the average values of the data points for a given L_{post}/L_0.

at which the post lattice is commensurate with an unstrained BCP microdomain lattice.

The predictions of this model were tested by preparing templates with the range of L_{post} = 66 to 184 nm (L_{post}/L_0 ~ 1.65 to 4.6) on a single substrate. Each template region consisted of posts covering a hexagonal area with a diameter of 4 μm. Having multiple templates on the same substrate ensured a uniform BCP film thickness (and hence the same L_0) across all templates with different L_{post} values. SEM images often showed more than one BCP microdomain lattice orientation within each post array. Image analysis was used to determine the (x, y) coordinates and Wigner-Seitz cells for each BCP lattice site. The area and orientation of each Wigner-Seitz cell were calculated to determine the area fraction of each BCP lattice (see SOM section S4). Figure 3B shows the area fraction of each lattice type as a function of the ratio L_{post}/L_0.

The experimental results and theoretical predictions in Fig. 3 agree closely. All the predicted lattice types, ⟨*1 1*⟩, ⟨*2 0*⟩, ⟨*2 1*⟩, ⟨*3 0*⟩, ⟨*2 2*⟩, ⟨*3 1*⟩, ⟨*4 0*⟩, ⟨*3 2*⟩, and ⟨*4 1*⟩, were observed as L_{post} varied. As expected, a particular lattice type dominated at the L_{post}/L_0 value for which the free-energy model predicted a minimum energy for that lattice type. We note that for the higher values of L_{post}/L_0, greater than ~3.5, there was no single BCP lattice orientation that completely filled the template, and all samples showed two or more different BCP lattice orientations. This effect can be understood as being due to the increasing width and number of the potential wells, such that the energy barriers separating different BCP orientations became smaller. A similar phenomenon was observed in previous work with BCP spheres packing in grooves, where N or N + 1 rows of spheres were observed to occur degenerately for wider grooves (*16*). For L_{post}/L_0 less than ~3.5, two lattice types also occurred simultaneously when L_{post}/L_0 was intermediate between values corresponding to energy minima.

Central to this work is the possibility of control of the final self-assembled lattice by design of the template parameters. The analysis above showed how a given BCP microdomain lattice ⟨*i j*⟩ could be selected by choice of L_{post}/L_0 and predicted what strain the BCP microdomain lattice experienced when fitting the post lattice. However, it did not address selection between degenerate lattice orientations. For example, two variants of lattice ⟨*2 1*⟩ could be formed when L_{post}/L_0 ~ 2.6, with orientations of θ = +19° or –19°, as shown in Fig. 4A. For a 6-fold symmetric post lattice, no preference for either orientation was observed. However, a preference could be established by adding posts that occupied microdomain lattice sites of only one of the possible variants. Figure 4B shows a defect-free BCP microdomain lattice that was formed using a sparse post arrangement that selected for a unique BCP orientation. The template was formed by removing posts from the original periodic post lattice and adding posts that matched only the desired BCP ⟨*2 1*⟩ lattice variant, while maintaining the overall post areal density. Templates were also designed to reduce the incidence of one lattice type, for example ⟨*2 1*⟩, compared with a competing orientation such as ⟨*3 0*⟩, by changing the motif present at each post lattice site. Figure 4, C and D, shows how this was accomplished by a template whose motif consisted of pairs of posts. A template of single posts showed a gradual transition between ⟨*2 1*⟩ and ⟨*3 0*⟩ lattices as L_{post}/L_0 increases from 2.8 to 3.0. However, with the post pair motif, the ⟨*2 1*⟩ orientation was frustrated and occupied a smaller area fraction of the substrate, even at L_{post}/L_0 = 2.6, where ⟨*2 1*⟩ gave the optimum lattice match with the template. Note also that the quality of the BCP microdomain lattice is relatively insensitive to the exact shape and size of the posts. Figure 4, E to G, shows well-ordered ⟨*3 0*⟩ lattices formed on three templates with identical period but differing post size and shape: 15-nm diameter, 25-nm diameter, and 45-nm × 25-nm ellipses. This tolerance is useful because it lowers the precision requirements on the template fabrication process.

In nontemplated films, the largest defect-free regions observed were on the order of 0.4 μm × 0.4 μm. On the other hand, in the templated case, defect-free arrays were observed over 2 μm or greater distances for L_{post}/L_0 < ~3. In cases where only one BCP lattice orientation existed, any defects that did occur did not disrupt the long-range orientation of the array, because the self-assembled structure remained in phase with the periodic boundary condition introduced by the template: Any point defect that occurred affected only the coordination number and spacing of nearby spherical domains. In the templated arrays, as the BCP microphase-separated, close-packed regions of domains are assumed to have nucleated around the posts, grown, and impinged; because the orientation of these small regions was fixed by the template, this locally registered nucleation of the lattice led to a macroscopically ordered BCP array, with some local regions having pairs of 5 and 7 coordinated spheres. This situation contrasts with the case of untemplated arrays, where such point defects would lead to a polycrystalline BCP microdomain lattice structure and a loss of long-range correlation. For larger L_{post}/L_0, we observed a slightly larger defect fraction, leading to coexistence of different BCP lattices and the presence of defects associated with their boundaries.

Although this work was performed using a spherical morphology PS-*b*-PDMS diblock copolymer, we expect the technique also to be appropriate for block copolymers with perpendicular cylindrical morphology, or lamellar structures. Indeed, the perpendicular cylinder morphology, which lacks the ability to adjust the positions of its domains along the direction normal to the

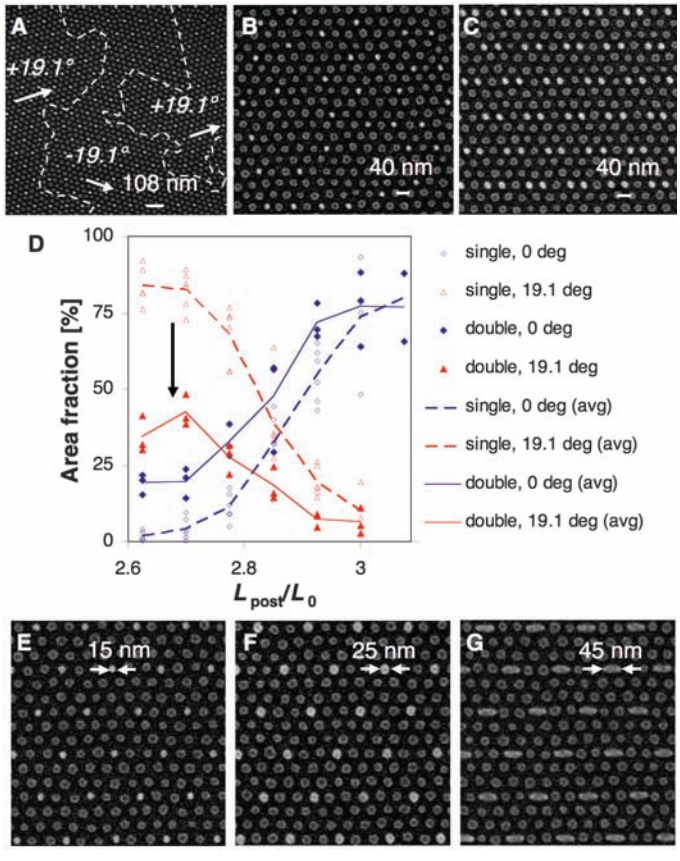

Fig. 4. (**A**) SEM image showing two degenerate ⟨*2 1*⟩ BCP microdomain lattice orientations (i.e., +19.1° and –19.1°) forming on one post lattice. The white dashed lines represent grain boundaries, and the arrows show the grain orientations. The periodic post lattice is commensurate with both orientations. (**B**) SEM image of a unique BCP microdomain lattice orientation obtained by breaking the periodicity of the post template. (**C**) A motif consisting of a pair of posts frustrates the formation of BCP lattice orientations other than the 0° ⟨*3 0*⟩ lattice. (**D**) A plot of area fraction versus L_{post}/L_0 for two template designs, single-post and double-post lattices. The double-post lattice template frustrates the 19.1° ⟨*2 1*⟩ orientation. (**E** to **G**) SEM images showing well-ordered BCP ⟨*3 0*⟩ arrays guided by pillars of different sizes [(E) and (F)] and shape (G) but with equal center-to-center spacing of 120 nm.

surface, may produce arrays with better placement accuracy than the accuracy demonstrated here, as well as higher aspect ratio features. Well-ordered block copolymer arrays may be useful as etch masks in a range of applications, such as patterned recording media, that require periodic nanoscale features covering large areas. This templating approach thus provides a method of combining top-down and bottom-up nanopatterning techniques, where information is placed on the substrate by writing a sparse lattice of posts, and the self-assembling material spontaneously populates the empty spaces on the template with a seamless nanostructured array of determined orientation and lattice spacing.

References and Notes

1. C. D. Bain *et al.*, *J. Am. Chem. Soc.* **111**, 321 (1989).
2. B. O. Dabbousi, C. B. Murray, M. F. Rubner, M. G. Bawendi, *Chem. Mater.* **6**, 216 (1994).
3. Y. Yin, Y. Xia, *Adv. Mater.* **13**, 267 (2001).
4. M. J. Fasolka, A. M. Mayes, *Annu. Rev. Mater. Res.* **31**, 323 (2001).
5. P. Mansky, P. Chaikin, E. L. Thomas, *J. Mater. Sci.* **30**, 1987 (1995).
6. M. Park, C. Harrison, P. M. Chaikin, R. A. Register, D. H. Adamson, *Science* **276**, 1401 (1997).
7. R. G. H. Lammertink *et al.*, *Adv. Mater.* **12**, 98 (2000).
8. T. Thurn-Albrecht *et al.*, *Science* **290**, 2126 (2000).
9. J. Y. Cheng *et al.*, *Adv. Mater.* **13**, 1174 (2001).
10. Y. S. Jung, C. A. Ross, *Nano Lett.* **7**, 2046 (2007).
11. C. Park, J. Yoon, E. L. Thomas, *Polymer* **44**, 6725 (2003).
12. R. A. Segalman, *Mater. Sci. Eng. Rep.* **48**, 191 (2005).
13. S. B. Darling, *Prog. Polym. Sci.* **32**, 1152 (2007).
14. R. A. Segalman, H. Yokoyama, E. J. Kramer, *Adv. Mater.* **13**, 1152 (2001).
15. J. Y. Cheng, C. A. Ross, E. L. Thomas, H. I. Smith, G. J. Vancso, *Appl. Phys. Lett.* **81**, 3657 (2002).
16. J. Y. Cheng, A. M. Mayes, C. A. Ross, *Nat. Mater.* **3**, 823 (2004).
17. L. Rockford *et al.*, *Phys. Rev. Lett.* **82**, 2602 (1999).
18. S. O. Kim *et al.*, *Nature* **424**, 411 (2003).
19. E. W. Edwards, M. F. Montague, H. H. Solak, C. J. Hawker, P. F. Nealey, *Adv. Mater.* **16**, 1315 (2004).
20. M. P. Stoykovich *et al.*, *Science* **308**, 1442 (2005).
21. J. Y. Cheng, C. T. Rettner, D. P. Sanders, H. C. Kim, W. D. Hinsberg, *Adv. Mater.*, published online 7 July 2008; 10.1002/adma.200800826.
22. R. Ruiz *et al.*, *Science* **321**, 936 (2008).
23. J. K. W. Yang, K. K. Berggren, *J. Vac. Sci. Technol. B* **25**, 2025 (2007).
24. G. J. Kellogg *et al.*, *Phys. Rev. Lett.* **76**, 2503 (1996).
25. D. J. Kinning, E. L. Thomas, *Macromolecules* **17**, 1712 (1984).
26. E. Helfand, *Acc. Chem. Res.* **8**, 295 (1975).
27. P. G. de Gennes, *Macromolecules* **13**, 1069 (1980).

28. The financial support of the National Science Foundation, the Semiconductor Research Corporation, the Nanoelectronics Research Initiative, King Abdullaziz City for Science and Technology and Alfaisal University, and the Singapore-MIT Alliance is appreciated. The Research Laboratory of Electronics Scanning-Electron-Beam Lithography Facility was used for this work. We thank M. Mondol and J. Daley for technical assistance. The authors declare no competing interests.

Supporting Online Material

www.sciencemag.org/cgi/content/full/321/5891/939/DC1
Materials and Methods
SOM Text
Figs. S1 and S2
Tables S1 and S2
References

21 April 2008; accepted 11 July 2008
10.1126/science.1159352

X-ray Diffraction and Computation Yield the Structure of Alkanethiols on Gold(111)

A. Cossaro,[1] R. Mazzarello,[2] R. Rousseau,[2]* L. Casalis,[3] A. Verdini,[1] A. Kohlmeyer,[4] L. Floreano,[1] S. Scandolo,[5] A. Morgante,[1,6]† M. L. Klein,[4] G. Scoles[2,3,7]

The structure of self-assembled monolayers (SAMs) of long-chain alkyl sulfides on gold(111) has been resolved by density functional theory–based molecular dynamics simulations and grazing incidence x-ray diffraction for hexanethiol and methylthiol. The analysis of molecular dynamics trajectories and the relative energies of possible SAM structures suggest a competition between SAM ordering, driven by the lateral van der Waals interaction between alkyl chains, and disordering of interfacial Au atoms, driven by the sulfur-gold interaction. We found that the sulfur atoms of the molecules bind at two distinct surface sites, and that the first gold surface layer contains gold atom vacancies (which are partially redistributed over different sites) as well as gold adatoms that are laterally bound to two sulfur atoms.

Self-assembled monolayers (SAMs) of alkyl sulfides on metal surfaces have many potential applications in molecular electronics, biosensors, and nanopatterning (*1*–*3*). In the high-coverage regime, the molecules are anchored to the metal substrate through their sulfur termination S, and the alkyl chains R [where R = $(CH_2)_nCH_3$] point away from the surface. Gold is the most commonly used substrate in sulfur-containing SAMs, in part because of the strong Au-S interaction.

However, despite many years of research on these systems, the nature of the Au-S interaction is still debated. Only recently has the role of the underlying Au substrate in the chemisorption of thiols been recognized, for both crystal and nanoparticle (NP) surfaces (*4*–*7*). For the short-chain limit (R = CH_3), the presence of adatoms and vacancies plays a crucial role in this process. Surface complexes wherein two S atoms are joined by an intermediate Au adatom (RS-Au-SR) have been observed experimentally at both low (*4*) and high coverage (*5*); this finding has been supported, and in certain cases predicted, by density functional theory (DFT) (*5*, *8*, *9*). Similar Au-SR motifs were recently identified at the surface of thiol-protected Au NPs (*10*).

It is natural to assume that these species are also present at the Au-SR interface of the long-chain SAMs (*11*). We now show that the energetics of the gold-SAM interface, in competition with the molecular packing forces arising from the alkyl chains at high coverage, lead to the formation of a commensurate superstructure, conventionally known as *c*(4×2) (*12*), in which the hydrocarbon chains tilt by about 30° from the surface normal. This structure yields the close packing that provides these SAMs with their technologically useful "passivating" properties (*2*, *13*–*15*).

Most of the structural models proposed so far for the *c*(4×2) superstructure have assumed that the Au(111) substrate remains flat and defect-free; they explain the superstructure in terms of nonequivalent chain torsion angles (*16*), sulfur dimerization (*15*), or differences in adsorption sites (*7*, *17*) [for a review, see (*18*)]. Only a few experimental investigations have been interpreted in terms of a more complex landscape at the interface. The alternatives included an Au atom rippling (*19*) and an increase in either the substrate roughness (*20*) or the density of defects (*21*). A recent theoretical study of intermediate-length alkyl sulfides on Au(111), which started from the results obtained in our previous work for CH_3S [methylthiol (MT)] SAMs (*5*), found that the RS-Au-SR motif is also energetically competitive for SAMs of the SC_nH_m moiety on Au(111) surfaces and is consistent with SAM corrugations seen in scanning tunneling microscopy (STM) images (*22*).

Here, we show that the existence of the RS-Au-SR structural motif for the case of longer alkanethiols is confirmed by a DFT-based theoretical simulation of the system that includes the lateral van der Waals interactions between the alkyl chains, as well as by a thorough analysis of extensive grazing incidence x-ray diffraction (GIXRD) experiments. Furthermore, DFT-based molecular dynamics (MD) simulations reveal the

[1]Istituto Nazionale per la Fisica della Materia–Consiglio Nazionale delle Ricerche (INFM-CNR) Laboratorio TASC, I-34012 Trieste, Italy. [2]International School for Advanced Studies, I-34014 Trieste, Italy. [3]Sincrotrone Trieste S.C.p.A., I-34012 Trieste, Italy. [4]Center for Molecular Modeling and Department of Chemistry, University of Pennsylvania, Philadelphia, PA 19104, USA. [5]Abdus Salam International Centre for Theoretical Physics and INFM/Democritos National Simulation Center, I-34014 Trieste, Italy. [6]Department of Physics, University of Trieste, I-34127 Trieste, Italy. [7]Department of Chemistry, Princeton University, Princeton, NJ 08544, USA.

*Present address: Pacific Northwest National Laboratory, Richland, WA 99352, USA.
†To whom correspondence should be addressed. E-mail: morgante@tasc.infm.it

Graphoepitaxy of Self-Assembled Block Copolymers on Two-Dimensional Periodic Patterned Templates

Ion Bita, Joel K. W. Yang, Yeon Sik Jung, Caroline A. Ross, Edwin L. Thomas and Karl K. Berggren (August 15, 2008)

Science **321** (5891), 939-943. [doi: 10.1126/science.1159352]

Editor's Summary